AGU PUBLICATIONS

JGR

Journal of Geophysical Research: Solid Earth

RESEARCH ARTICLE
10.1002/2017JB014400

Key Points:
- Established, for the first time, the flow law for diffusion creep of enstatite under hydrous conditions
- Discussed the rheology contrast between olivine and enstatite, the dominant minerals in the upper mantle
- The viscosity of enstatite in water-rich regions can be 2 order of magnitude lower than that in water-poor regions

Correspondence to:
M. Song & S. Mei,
mei@sidsse.ac.cn;
msong@gig.ac.cn

Citation:
Zhang, G., Mei, S., Song, M., & Kohlstedt, D. L. (2017). Diffusion creep of enstatite at high pressures under hydrous conditions. *Journal of Geophysical Research: Solid Earth*, *122*, 7718–7728. https://doi.org/10.1002/2017JB014400

Received 2 MAY 2017
Accepted 25 SEP 2017
Accepted article online 4 OCT 2017
Published online 21 OCT 2017

©2017. American Geophysical Union. All Rights Reserved.

Diffusion Creep of Enstatite at High Pressures Under Hydrous Conditions

Guinan Zhang[1,2,3], Shenghua Mei[4,3], Maoshuang Song[1], and David L. Kohlstedt[3]

[1]State Key Laboratory of Isotope Geochemistry, Guangzhou Institute of Geochemistry, Chinese Academy of Sciences, Guangzhou, China, [2]Department of Earth Sciences, University of Chinese Academy of Sciences, Beijing, China, [3]Departments of Earth Sciences, University of Minnesota, Twin Cities, Minneapolis, MN, USA, [4]CAS Key Laboratory for Experimental Study under Deep-sea Extreme Conditions, Institute of Deep-sea Science and Engineering, Chinese Academy of Sciences, Sanya, China

Abstract Mantle convection and large-scale plate motion depend critically on the nature of the lithosphere-asthenosphere boundary and thus on the viscosity structure of Earth's upper mantle, which is determined by the rheological properties of its constituent minerals. To constrain the flow behavior of orthopyroxene, the second most abundant constituent of the upper mantle, deformation experiments were carried out in triaxial compressive creep on fine-grained (~6 μm) samples of enstatite at high pressures (3.8–6.3 GPa) and high temperatures (1323–1573 K) using a deformation-DIA apparatus. Based on results from this study, the deformation behavior of enstatite is quantitatively presented in the form of a flow law that describes the dependence of deformation rate on differential stress, water fugacity, temperature, and pressure. Specifically, the creep rate depends approximately linearly on stress, indicating deformation in the diffusion creep regime. A least squares regression fit to our data yielded a flow law for diffusion creep with an activation energy of ~200 kJ/mol and an activation volume of ~14×10^{-6} m^3/mol. The magnitude of the water-weakening effect is similar to that for olivine with a water fugacity exponent of $r \approx 0.7$. This strong dependence of viscosity on water fugacity (concentration) indicates that the viscosity of an orthopyroxene-bearing mantle varies from one geological setting to another, depending on the large-scale water distribution. Based on the rheology contrast between olivine and enstatite, we conclude that olivine is weaker than enstatite throughout most of the upper mantle except in some shallow regions in the diffusion creep regime.

1. Introduction

The flow behavior of the upper mantle is determined by the rheological properties of its constituent minerals, including olivine, orthopyroxene (opx), and clinopyroxene. Though opx makes up approximately 25% of Earth's upper mantle, next only to olivine (Ringwood, 1975), and is an important mineral in the other terrestrial planets (Burns, 1989; Mocquet et al., 2011; Sanloup et al., 1999), relatively little emphasis has been given to experimental investigation of its rheological properties.

Both scientific and technological challenges exist for quantifying the rheological behavior of opx. In the former, the rheological properties of opx have largely been overlooked because the most abundant mineral of the upper mantle, olivine, has been assumed to be the least viscous phase that therefore controls mantle flow behavior. However, this perspective might be incomplete or even inappropriate because recent studies have demonstrated that at least under some conditions, opx is weaker than olivine (Ohuchi et al., 2011). In addition, plastic deformation in the lithosphere is often localized, a behavior promoted by a "soft" secondary phase such as opx (Warren & Hirth, 2006). Furthermore, observations from some deep mantle xenoliths suggest that at certain conditions opx may play a significant role in deformation (Skemer & Karato, 2007). Thus, a thorough understanding of the rheological behavior of opx is of significant importance in exploring mantle flow.

In the latter, the maximum working pressure of gas-medium presses with high resolution in stress, strain rate, and temperature is below that required for remaining in the stability field of opx at high temperatures. Apparatuses capable of deformation experiments at higher pressures lack high resolution in stress. As a result, published results on the creep behavior of opx are not only few but also scattered, and existing experimental studies have focused on dislocation creep (e.g., Bystricky et al., 2016; Mackwell, 1991; Ohuchi et al., 2011; Raterron et al., 2016) with little published work on the diffusion creep behavior of opx.

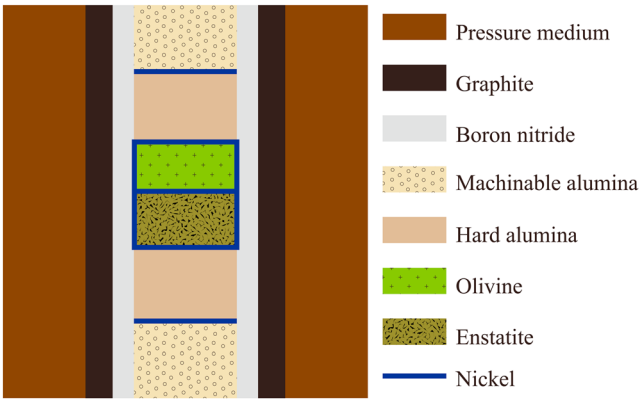

Figure 1. Sketch of sample assembly (not to scale) used for deformation experiments.

Diffusion creep is potentially a deformation mechanism of significant importance to deep Earth's dynamics. Extrapolation of laboratory flow laws to mantle condition suggests that the deformation of the upper mantle occurs close to the boundary between diffusion and dislocation creep regimes (e.g., Hirth & Kohlstedt, 2003). Geological observations reveal that even though opx frequently deforms by dislocation creep in tectonites (e.g., Etheridge, 1975; Skemer et al., 2010; Soustelle et al., 2009; Tikoff et al., 2010), some microstructure and fabric signatures in peridotites indicate that diffusion creep of opx plays an important role in the deformation within Earth's interior (e.g., Dijkstra et al., 2002; Linckens et al., 2011; Toy et al., 2010). For example, the disappearance of seismic anisotropy below the Lehmann discontinuity (~200 km) has been attributed to a transition in deformation mechanism from dislocation to diffusion creep (Karato, 1992). Furthermore, diffusion creep might be important in the shallow upper mantle, as suggested by recent studies that demonstrate that crystallographic preferred orientations can be induced or preserved during diffusion creep (Jiang et al., 2000; Miyazaki et al., 2013; Skemer & Karato, 2008; Wheeler, 2009). Although several experimental investigations of the diffusion creep regime of olivine, until now, only Tasaka et al. (2013) performed compression experiments to study diffusion creep of iron-free, fine-grained enstatite aggregates. However, these studies did not quantify the effects of pressure and water fugacity, both of which are influence the extrapolation of experimental measured flow laws to geological settings.

Water dissolved as hydrogen in nominally anhydrous minerals, such as opx, is a common phenomenon (Bell et al., 1995; Gose et al., 2009; Peslier et al., 2002), one that is important for water weakening of many nominally anhydrous silicate minerals (Mei & Kohlstedt, 2000; Hier-Majumder et al., 2005; Xu et al., 2013). However, no experimental investigation of the effect of water on the flow behavior of opx has yet been reported. Therefore, it is critical to quantify the influence of water on the creep behavior of opx in order to estimate the rheological properties of opx in hydrous region of the upper mantle.

In this study, we carried out a series of creep experiments on polycrystalline enstatite using a deformation-DIA (D-DIA) apparatus at high temperatures ($1323 \leq T \leq 1573$ K) and high pressures ($3.8 \leq P \leq 6.3$ GPa) to ensure that enstatite deforms fully in the orthoenstatite stability field. These experiments explore the rheological behavior of enstatite under hydrous conditions at the high pressure-temperature (*P-T*) conditions appropriate to the upper mantle. The purpose of this research was to measure the flow law for diffusion creep of enstatite, particularly quantifying the influence of pressure and water fugacity, so as to constrain further the viscosity structure of Earth's upper mantle.

2. Experimental Methods

2.1. Sample Preparation and Assembly

Polycrystalline samples were fabricated from powdered natural enstatite from Bamble, Norway. The chemical composition of the enstatite is approximately $(Mg_{0.85}Fe_{0.14}Al_{0.005}\ Ca_{0.005})\ SiO_3$, analyzed with an electron microprobe (JEOL JXA-8900R) in the Department of Earth Sciences, University of Minnesota.

Samples 1 mm in diameter and ~0.8 mm in length were prepared by either cold pressing or hot pressing. In the former, fine-grained enstatite powder with a particle size of ~15–25 μm was cold pressed into a column with designated dimensions using a table vise; in the latter, enstatite powder was first hot pressed using a gas-medium press at 300 MPa and 1473 K for 3 h, resulting in a dense rod ~9 mm in diameter. Samples of desired diameter for D-DIA experiments were then cored from the hot-pressed rod with a diamond coring drill.

For deformation experiments, each cold- or hot-pressed cylindrical sample (~0.8 mm in length and 1.0 mm in diameter) stacked with a San Carlos olivine sample of similar size was assembled with a graphite resistance heater, a boron nitride sleeve, and alumina pistons into a 6.2 mm edge length cubic pressure medium of boron-epoxy resin, as illustrated in Figure 1. The enclosed olivine sample served as a standard for stress

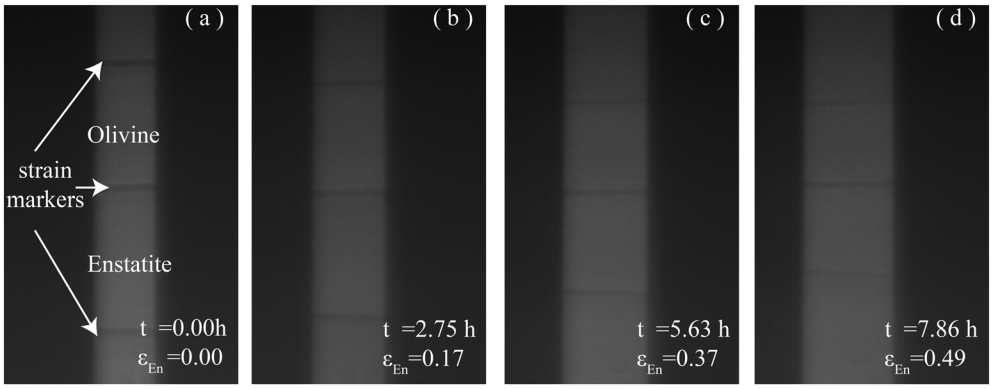

Figure 2. Time-resolved X-ray radiographs of the sample column for a deformation experiment (San_337): (a) $t = 0.00$ h, $\varepsilon_{En} = 0.00$; (b) $t = 2.75$ h, $\varepsilon_{En} = 0.17$; (c) $t = 5.63$ h, $\varepsilon_{En} = 0.37$; (d) $t = 7.86$ h, $\varepsilon_{En} = 0.49$. Plastic strain of the deforming sample is deduced from these recorded radiographs.

measurement using X-ray diffraction. Samples were wrapped with Ni foil of 25 μm thicknesses for buffering the oxygen fugacity. Nickel disks of similar thickness were placed between each end of the enstatite and olivine samples as strain markers for monitoring length change of samples in situ with radiography.

2.2. Deformation Experiment

Triaxial compressive creep experiments were carried out at high temperatures and high pressures using a D-DIA apparatus at a synchrotron X-ray beamline (NSLS, Brookhaven National Lab, and APS, Argonne National Lab). At the beginning of each experiment, the sample assembly was first pressurized hydrostatically to the desired value, and subsequently, the temperature was increased to the target level. The temperature during the experiments was determined based on calibrations of furnace power versus temperature using identical assemblies prepared with a thermocouple. After both pressure and temperature arrived at the target values, the samples were annealed for at least half an hour to let the temperature and pressure stabilize.

During deformation experiments, a high-intensity beam of white X-rays passed through the deforming sample assembly so that time-resolved X-ray radiographies of the enstatite and olivine samples as well as X-ray diffraction patterns of olivine could be periodically collected in situ. Radiographies, such as those in Figure 2, taken along the sample column during deformation provided information on the change in length of the two samples as a function of time, information necessary for the calculation of strain and strain rate.

X-ray diffraction patterns of olivine collected simultaneously on detectors aligned around the incident beam permitted the evaluation of lattice spacing within the sample both parallel to and perpendicular to the loading axis. This information was used to determine the mean stress (confining pressure) and the differential stress within the deforming sample (e.g., Singh, 1993; Singh et al., 1998). In this study, stress and pressure were deduced from the sharpest diffraction peaks (hkl = 112, 130, and 131) of the olivine diffraction patterns. Details of this technique are discussed in previous papers (Li et al., 2004; Mei et al., 2008).

In general, a run consisted of a few steps at several temperatures or pressures with deformation halted between steps. The differential stress approached a quasi steady state value at a strain of over 10%, as demonstrated in Figure 3.

2.3. Water Content Analysis

The water content in the deformed samples was analyzed using Fourier transform infrared (FTIR) spectroscopy. Since the pressure medium for our sample assembly was made of boron-epoxy resin, water was released through decomposition of the epoxy at temperatures of >473 K. A trace amount of water is enough to saturate nominally anhydrous minerals such as olivine and enstatite used in our deformation experiments. To examine the water content of our samples, the deformed samples were cut parallel to the compression direction and double polished to a thickness of 200 to 300 μm with diamond lapping film down to a 1 μm finish. The water concentration of enstatite and olivine was determined from unpolarized infrared spectra collected with a Bruker Tensor 37 Fourier transform infrared spectrometer. All measurements were carried out with a continuous stream of dried air to purge the sample chamber of the microscope using an

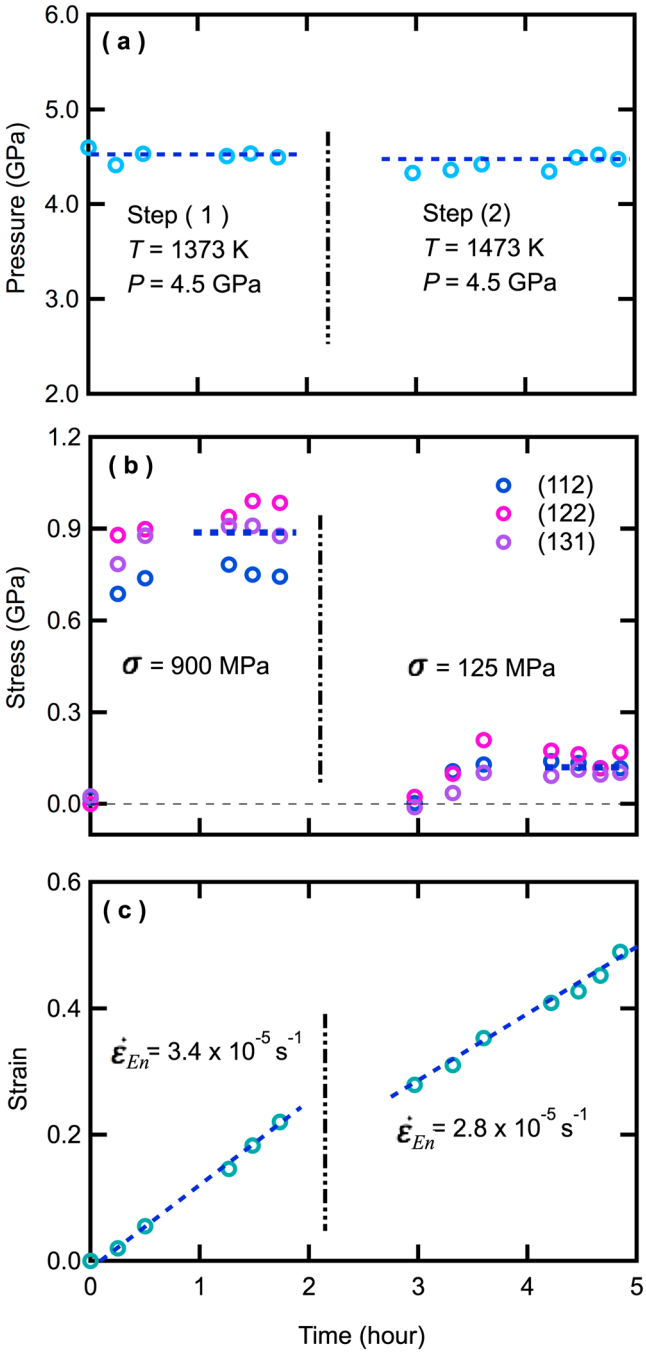

Figure 3. Plots of (a) pressure, (b) stress, and (c) strain rate versus elapsed time for run San_309. The stress and pressure were deduced from three diffraction peaks ((*hkl*) = (112), (122), and (131)) of olivine. The strain rate for enstatite was calculated from time-resolved radiographs.

aperture with an area of approximately 60 × 60 μm^2. All spectra were obtained at wave numbers between 2,400 and 4,000 cm^{-1}. Five infrared spectra of each sample, from the center to the edge of the sample, were collected with 256 scans at resolution of 2 cm^{-1}. Water contents within samples were computed using the Paterson calibration (Paterson, 1982) by integrating IR absorption intensities between 3,000 and 3,750 cm^{-1}:

$$C_{OH} = \frac{\Omega}{150\xi}\int \frac{H(\nu)}{(3780-\nu)}d\nu \ , \quad (1)$$

where C_{OH} is the hydroxyl content in H/10^6 Si. Ω, the molar volume, is 4.4 × 10^4 mm^3/mol for olivine and 6.3 × 10^4 mm^3/mol for enstatite. The orientation factor, ξ, is equal to 1/3 for unpolarized spectra of polycrystalline samples. $H(\nu)$ is the absorption coefficient at wave number ν.

3. Experimental Results

Eighteen deformation experiments were conducted on eight samples at high temperatures (1323 ≤ T ≤ 1573 K) and high pressures (3.8 ≤ P ≤ 6.3 GPa). Table 1 summarizes all run conditions and experimental results.

3.1. Water Content and Water Fugacity

All the unpolarized FTIR spectra from olivine and enstatite are presented in Figure 4. Based on these results, water contents in both olivine and enstatite tend to increase with increasing pressure. Enstatite aggregates incorporate much more hydrogen than olivine under the same *P-T* conditions. The partition coefficient for water between olivine and enstatite aggregates, $C_{H_2O}^{olivine}/C_{H_2O}^{enstatite}$, is ~0.5, which agrees well with the observation of Fabbrizio et al. (2013). With the availability of the water content in olivine from each run, the water fugacity for the run can be estimated based on the well-determined relationship between water content and water fugacity for olivine (Kohlstedt et al., 1996; Zhao et al., 2004). In the estimation, a factor of 3.5 was used to transfer the water content from the Paterson calibration (Paterson, 1982) to the Bell calibration (Bell et al., 2003). The estimated water fugacity associated with the last step of each run is given in Table 1.

3.2. Microstructural Observations

Deformed samples were cut into pieces along their compression axis in order to prepare thin sections and scanning electron microscopy (SEM) samples for microstructural analyses. Each sample slice was ground on diamond lapping films to 1 μm and then polished with SYTON fluid (0.05 μm colloidal silica) for about 6 h. Samples were analyzed at the China University of Geosciences in Wuhan with a field emission gun scanning electron microscope (FEI Quanta FEG-SEM 450) coupled with an electron backscatter diffraction (EBSD) system (NordlysII& Channel 5.0). In specific, orientation contrast images of each deformed sample were obtained by scanning the sample with the electron beams at a step size of 0.5 μm in order to reveal the distribution of grain orientations within samples. Typical orientation contrast images obtained from SEM-EBSD analyses for San_335 and San354 are shown in Figures 5a and 5b, respectively. To calculate grain size, we traced the enstatite grain boundaries on images. Then, with the help of the IMAGE SXM, we calculated the area(s) of each grain. The equivalent grain size (d) was then calculated from the formula of $d = 2\sqrt{(s/\pi)}$, which assumes spherical grains. With this

Table 1
Experimental Conditions and Results

Run no.	Temperature (K)	Pressure (GPa)	Stress (MPa)	Strain (%)[a]	Strain rate (s^{-1})	$C_{H_2O}^{enstatite}$ ($H/10^6Si$)[b]	$C_{H_2O}^{olivine}$ ($H/10^6Si$)[b]	f_{H_2O} (GPa)
San_309[c]	1373	4.5	900	18	3.43×10^{-5}			
	1473	4.5	125	48	2.79×10^{-5}	6,800	3,340	138
San_319[c]	1373	6.3	1,000	15	1.40×10^{-5}			
	1473	6.3	250	35	2.33×10^{-5}	15,000	4,160	745
San_335[d]	1373	4.1	190	15	1.58×10^{-5}			
	1473	3.8	100	32	2.33×10^{-5}			
	1573	3.5	50	48	2.94×10^{-5}			
San_337[d]	1373	6.1	570	20	1.42×10^{-5}			
	1473	5.7	150	37	1.88×10^{-5}			
	1573	5.2	100	51	2.88×10^{-5}	3,000	1,850	84
San_351[c]	1323	5	900	20	5.07×10^{-5}			
	1423	4.9	350	46	4.59×10^{-5}			
San_353[c]	1373	5.2	540	17	2.81×10^{-5}			
	1473	5.1	140	36	2.02×10^{-5}	5,300	3,000	202
San_354[c]	1423	3.9	270	15	2.18×10^{-5}			
	1523	3.9	100	31	3.29×10^{-5}	2,300	1,750	36
San_355[d]	1423	5.2	1300	20	5.58×10^{-5}			
	1523	4.9	440	52	9.03×10^{-5}	5,000	1,900	85

[a]Accumulated strain. [b]Water content calculated from enstatite and olivine aggregates using the weighted correction method of Paterson (1982). Experiments were carried out with [c]cold-pressed samples and [d]hot-pressed samples.

method, the grain sizes of San_335 and San354 are 6.4 μm and 5.9 μm, respectively. The frequency histograms of grain size distributions for those two samples are shown in Figures 5c and 5d. The average equivalent grain sizes (~6 μm) obtained from the optical photomicrographs through thin sections agree well with that obtained from orientation contrast images.

3.3. Mechanical Results

We analyzed our mechanical data in terms of a power law equation of the following form

$$\dot{\varepsilon}(\sigma, d, f_{H_2O}, T, P) = A\sigma^n d^{-m} f_{H_2O}^r \exp\left(-\frac{E+PV}{RT}\right), \quad (2)$$

where $\dot{\varepsilon}$ is the axial strain rate, A is the preexponential constant, σ is the differential stress, n is the stress exponent, d is the grain size, m is the grain size exponent, f_{H_2O} is the water fugacity, r is the water fugacity exponent, P is the confining pressure, T is the absolute temperature, E is the activation energy, V is the activation volume, and R is the gas constant.

As presented in Table 1, water fugacity and grain size are available only for the last step of each run. Hence, those data points were selected purposely for making the most reliable analyses of the mechanical properties of enstatite described by equation (2). Based on microstructural observations on orientation contrast images and optical photomicrographs that revealed that grain size in all of the deformed samples is relative small at ~6 μm, we assume that grain boundary diffusion creep is the dominant deformation mechanism in our experiments. In fact, a least squares regression fitting of our data to equation (2) yielded $n \approx 1$, a characteristic indication for the diffusion creep, supporting our assumption. Thus, by fixing $n = 1$ and $m = 3$, a further fitting to equation (2) yielded $E = 200 \pm 15$ kJ/mol, $V = (14 \pm 2) \times 10^{-6}$ m^3/mol, $r = 0.7 \pm 0.2$, and $A = 32$ s^{-1} $MPa^{-1.7}$ μm^3.

The dependence of the creep rate of enstatite on differential stress is plotted in a log-log plot in Figure 6a in which all the mechanical data obtained at different temperatures, pressures, and water fugacities were normalized to $T = 1473$ K, $P = 4.5$ GPa, and $f_{H_2O} = 10$ GPa, respectively, using equation (2) and the flow law parameters given in the previous paragraph. It has to be pointed out that the water fugacity at any step prior to the last one was estimated according to the water fugacity and *P-T* condition relationship of this study. The effect of water fugacity on the diffusion creep behavior of enstatite is explored in the log-log plot of strain

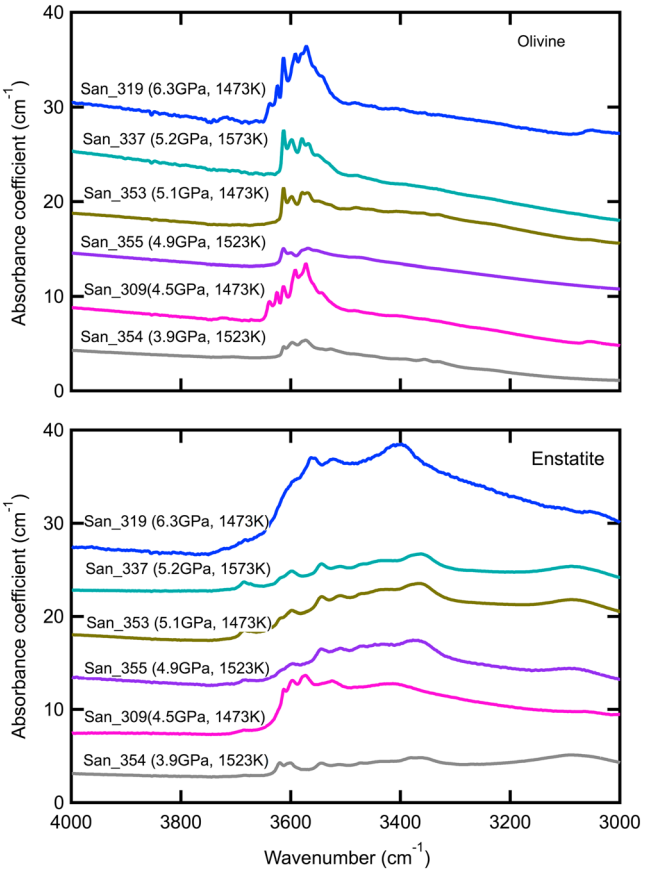

Figure 4. Fourier transform infrared spectra obtained from deformed olivine (top) and enstatite (bottom) samples. Experimental *P-T* conditions for each run are denoted for each spectrum. As illustrated, water contents in both olivine and enstatite tend to increase with increasing pressure.

rate versus fugacity, normalized to T = 1473 K, P = 4.5 GPa, and σ = 100 MPa in Figure 6b. In addition, the dependence of creep rate on temperature and pressure are illustrated in Figures 6c and 6d, respectively.

In Figure 6, the data are divided into two groups: the first group is composed of data obtained from the last step of each run (denoted in blue) in which grain size and water content were determined from quenched samples; these data points were used for a trial fitting. The second group is composed of data obtained from the step prior to the last one in which grain size and water content were estimated (denoted in pink). While the best fit lines were obtained from fits of only the first group of data, the second group is fairly well represented by the same fitting curves.

4. Discussions

4.1. Physical Processes of Deformation

At high temperatures, minerals deform by the operation of various processes including dislocation motion, grain boundary sliding, and ionic diffusion. In particular, diffusion processes are activated favorably in solids with fine grain sizes. In our experiments, as demonstrated in last section, fitting of the creep data associated with the last step of each run to the flow law expressed in equation (2) yields a stress exponent of $n \approx 1$, a characteristic index indicating that samples deformed in the diffusion creep regime. Meanwhile, microstructural observations of deformed samples, which were quenched after the completion of the last step of deformation of each experiment, reveal that our samples are composed of small grains with an average size of ~6 μm, favoring diffusion processes. Based on those facts, our microstructural and mechanical results are in good agreement.

It needs to note that our enstatite samples were fabricated from powders with a particle size of ~15–25 μm. This fact indicates that grain size refinement processes occurred at some stage before the last step of deformation in each experiment. Grain size refinement may result from either powder crushing during pressurization or dynamic recrystallization during deformation. Our samples were deformed at a constant strain rate; thus, if any dynamic recrystallization occurs, it should result in a drop of differential stress. However, as shown in Figure 3, no stress drop was observed. Furthermore, as shown in Figure 6, fitting of data from both the first and second steps of each run yields a stress exponent of ~1, indicating that samples deformed in the diffusion creep regime. Thus, it is unlikely that a significant amount of dynamic recrystallization occurred during deformation.

4.2. Effect of Water

Creep rate of a nominally anhydrous silicate minerals is significantly enhanced by the presence of water, as documented for several mantle minerals, including olivine, clinopyroxene, and garnet (Chen et al., 2006; Hier-Majumder et al., 2005; Karato et al., 1986; Mei & Kohlstedt, 2000; Xu et al., 2013). In general, transport properties including ionic diffusion in solids are governed by the point defect structure, which is influenced by chemical environment. In specific, the presence of water at high temperatures results in the presence of water-derived point defects such as protons (H^+) and hydroxyl ions (OH^-). The increase in the concentration of intrinsic point defects in a solid containing water-derived point defects changes the point defect chemistry for the solid and, as a consequence, the transport properties of the solid.

To analyze the point defect thermodynamics of enstatite under hydrous conditions, a theoretical framework is presented in Table 2. In the discussion that follows, the Kröger-Vink notation is used to indicate species, charge, and site occupancy for point detects (Kröger & Vink, 1956).

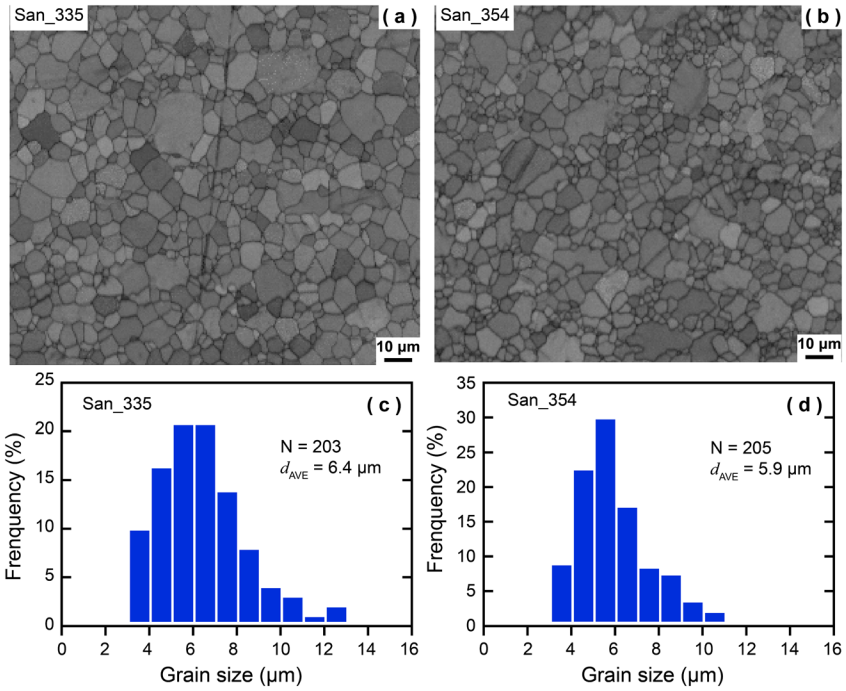

Figure 5. (a and b) Orientation contrast images and (c and d) frequency histograms of grain size for deformed samples (San_335 and San_354). The average grain size is ~6 μm based on analysis of ~200 grains.

Our experimental results indicate that diffusion creep of enstatite depends on water fugacity to the ~2/3 power. The concentration of the rate limiting species in the diffusion process should have similar water fugacity dependence. Fisler et al. (1997) argued that silicon grain boundary diffusion is most likely the rate limiting species. Then, based on Table 2, there are two cases that satisfy the experimental observations: (1) silicon

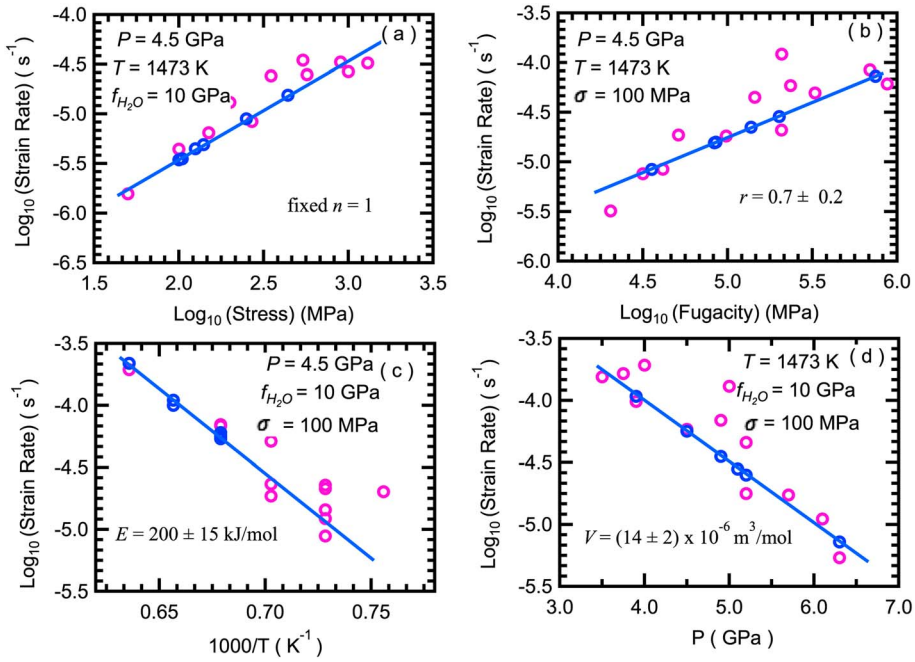

Figure 6. Creep results for enstatite: (a) log-log plot of strain rate versus stress; (b) log-log plot of strain rate versus water fugacity; (c) Arrhenius plot of log strain rate versus inverse temperature; and (d) plot of log strain rate versus pressure. Blue circles illustrate the data obtained from the last step of each run, while pink circles show the data from the runs prior to the last step.

Table 2
The Dependencies of the Concentrations of Intrinsic Point Defects on Water Fugacity, [] ∝ $f^r_{H_2O}$, for Enstatite for Various Charge Neutrality Conditions

	Diffusion species					
Charge neutrality conditions	$[V''_{Me}]$	$[Me_i^{\cdot\cdot}]$	$[V_o^{\cdot\cdot}]$	$[O_i'']$	$[V_{Si}''''']$	$s[Si_i^{\cdot\cdot\cdot\cdot}]$
$[(OH)_o^{\cdot}] = 2[V''_{Me}]$	1/3	−1/3	−1/3	1/3	2/3	−2/3
$[(OH)_o^{\cdot}] = [H'_{Me}]$	0	0	0	0	0	0
$[Fe_{Me}^{\cdot}] = [H'_{Me}]$	−1/2	1/2	1/2	−1/2	−1	1
$[Fe_{Me}^{\cdot}] = 3[H'''_{Si}]$	−1/4	1/4	1/4	−1/4	−1/2	1/2
$[Fe_{Me}^{\cdot}] = 2[(2H)''_{Me}]$	−2/3	2/3	2/3	−2/3	−4/3	4/3
$[Fe_{Me}^{\cdot}] = [(3H)'_{Si}]$	−3/2	3/2	3/2	−3/2	−3	3
$[(OH)_o^{\cdot}] = 3[H'''_{Si}]$	0	0	0	0	0	0
$[(OH)_o^{\cdot}] = 2[(2H)''_{Si}]$	−1/3	1/3	1/3	−1/3	−2/3	2/3
$[(OH)_o^{\cdot}] = [(3H)'_{Si}]$	−1	1	1	−1	−2	2

diffusing via a vacancy mechanism under the charge neutrality condition $[(OH)_O^{\cdot}] = 2[V''_{Me}]$ and (2) silicon diffusing via an interstitial mechanism under the charge neutrality condition $[(OH)_O^{\cdot}] = 2[(2H)''_{Si}]$. Detailed diffusion studies are required to carry this point defect analysis further.

The dependencies of the concentrations of various intrinsic point defects in opx on water fugacity are the same as those for olivine (Mei & Kohlstedt, 2000) for the same charge neutrality condition. Moreover, both olivine and enstatite belong to orthorhombic-dipyramidal crystal system and consist of the same elements. Hence, it may not be surprising that olivine and enstastite have a similar dependence of diffusion creep rate on water fugacity with a water fugacity exponent of 0.7.

4.3. Comparison With Previous Studies

The rheological properties of enstatite have not been well documented, especially its creep behavior in the diffusion creep regime. Tasaka et al. (2013) performed compression experiments to study diffusion creep of iron-free, fine-grained enstatite aggregates under anhydrous condition. In addition, Bruijn and Skemer (2014) examined the diffusion behavior of enstatite based partially on previous studies (e.g., Lawlis, 1998).

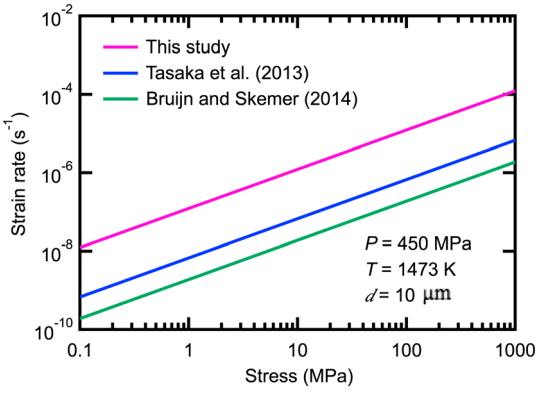

Figure 7. Comparison of diffusion creep results from this study carried out under hydrous conditions to those obtained under anhydrous conditions. Results of all studies were normalized to T = 1473 K, P = 450 MPa, and d = 10 μm.

A comparison of our results to these published results is given in Figure 7 with the experimental results normalized to T = 1473 K, P = 450 MPa, and d = 10 μm. We ignored the influence of pressure in normalizing the results of Tasaka et al. (2013) to the specified conditions, because the pressure in their experiments was relatively low (300 MPa) and similar to the normalization pressure. As shown in Figure 7, enstatite deformed under hydrous conditions (this study) crept ~2 orders of magnitude faster than enstatite deformed under anhydrous conditions (Bruijn & Skemer, 2014) at the same stress and temperature in the diffusion creep regime, indicating a strong water-weakening effect. The small difference in the creep strength of enstatite between the studies of Tasaka et al. (2013) and Bruijn and Skemer (2014) may result from the difference in composition of their samples (Fe-free versus Fe-bearing samples) or uncertainties in, for example, grain size.

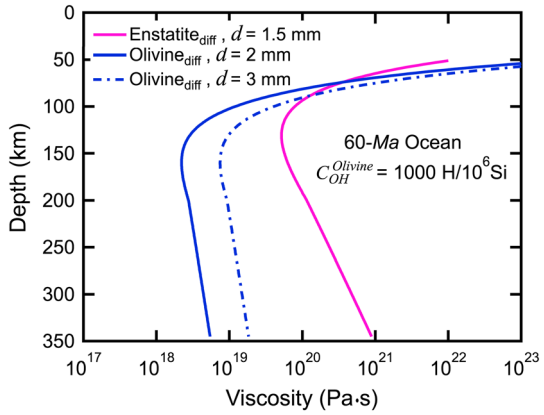

Figure 8. Viscosity-depth profile for the upper mantle estimated based on the flow law of enstatite from this study and that of olivine from Hirth and Kohlstedt (2003). In this plot, water fugacity is computed based on the relationship between water content and water fugacity for olivine determined by Zhao et al. (2004), and the oceanic geotherm is deduced following Turcotte and Schubert (2014, p.221). Water content of 1000 H/10^{6}Si of olivine is chosen based on Hirth and Kohlstedt (1996). The solid lines show viscosities predicted for diffusion creep (subscripted as diff) of enstatite and olivine with grain size of 1.5 mm and 2 mm, respectively. The dashed lines show viscosities predicted for diffusion creep of olivine with grain size of 3 mm.

4.4. Geological Implications

As stated above, olivine is often assumed to be weaker than opx and assumed to control the flow behavior of the mantle (Kohlstedt et al., 1995; Li & Gerya, 2009). However, this perspective lacks experimental constraints, especially in the diffusion creep regime. The viscosity of opx according to previous laboratory studies is not well constrained, with some studies suggesting that opx is more viscous than olivine (Bystricky et al., 2016; Hitchings et al., 1989; Mackwell, 1991) and others suggesting the opposite (Ohuchi et al., 2011; Raleigh et al., 1971; Ross & Nielsen, 1978). In addition, geochemical or geophysical studies indicate that some regions of the mantle are wet (Dixon et al., 2002, 2004; Huang et al., 2005; Karato, 2011; Maggi et al., 2000; Sobolev & Chaussidon, 1996) with water content varying regionally (Dixon et al., 2004; Huang et al., 2005). The flow law for diffusion creep of enstatite under hydrous conditions established by our study can be applied to provide constraints on viscosity envelopes of these regions in Earth's upper mantle.

To evaluate the viscosity ($\eta = \sigma/3\dot{\varepsilon}$) of hydrous regions in the upper mantle, the diffusion creep behavior of enstatite from this study and that of olivine from Hirth and Kohlstedt (2003) are plotted in Figure 8. The oceanic geotherm is from Turcotte and Schubert (2014, p.221). A water content of 1,000 H/10^{6}Si for olivine is chosen based on Hirth and Kohlstedt (1996). Grain sizes of 2 mm and 1.5 mm are chosen for olivine and enstatite, respectively, based on analyses of those two minerals in harzburgite and lherzolite xenoliths (Kukkonen & Peltonen, 1999). As shown in Figure 8, enstatite is less viscous than olivine at depths of $<$75 km in the oceanic lithosphere while, below this depth, olivine becomes less viscous than enstatite. It should be noted that the depth of relative viscosity transition between enstatite and olivine may shift slightly with stress, water content, and gran size. For example, if the grain size of olivine is 3 mm, the maximum grain size given by Kukkonen and Peltonen (1999), the viscosity transition depth changes from 75 to 90 km. Thus, it should not be taken for granted that olivine is more viscous than enstatite in all the regions of Earth's interior. Though our result does not conflict with the well-accepted understanding that the viscosity of the asthenosphere is dominated by olivine, it provides a necessary database for placing a better constraint on the rheological structure of Earth's upper mantle. It needs to be pointed out that the comparison illustrated in Figure 8 was made based only on the diffusion creep data available for both olivine and enstatite. Nevertheless, more sophisticated comparison should include contributions to deformation from other major mechanisms such as dislocation creep and disGBS; however, those properties for enstatite under hydrous conditions have not been quantified yet.

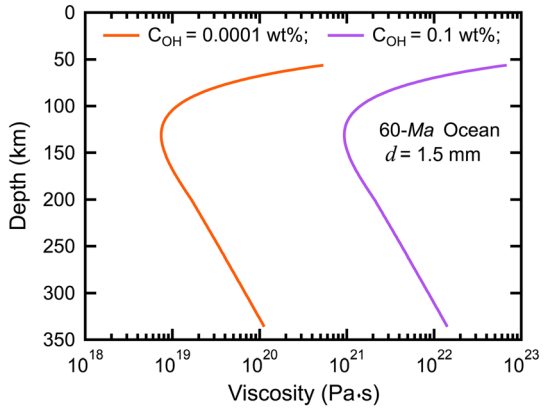

Figure 9. Viscosity-depth profile of the upper mantle for different water content estimated based on the flow law of enstatite from this study. The grain size of 1.5 mm is chosen based on Kukkonen and Peltonen (1999). Similar to Figure 8, water fugacity is computed based on the relationship between water content and water fugacity for olivine determined by Zhao et al. (2004), and the oceanic geotherm is deduced from Turcotte and Schubert (2014, p.221).

Based on the diffusion creep flow law for enstatite illustrated in Figure 9, at a depth of 125 km, the viscosity of the upper mantle in water-poor regions (e.g., cratons, water content $<$0.0001 wt %) and water-rich regions (e.g., subduction zones, water content $>$0.1 wt %) are ~10^{21} and ~10^{19} Pa s, respectively; that is, the difference in water concentration can exert variations in viscosity of up to 2 orders of magnitude. Thus, the variations of spatial water distribution are expected to make significant contributions to lateral variations in viscosity in the upper mantle, as inferred by Dixon et al. (2004).

In addition, the upper mantle consists of polymineralic rocks, and strictly, it is not appropriate to use the rheological properties of only one mineral, either olivine or opx, to represent flow its behavior. To provide more nuanced constraints on the viscosity structure of upper mantle, rheological properties of polyphase aggregates such as

olivine plus opx, two of the major constituent minerals of the upper mantle, need to be further investigated, and our results provide a foundation for such an end.

Acknowledgments
This research was supported by Strategic Priority Research Program (B) of Chinese Academy of Sciences (grants XDB18000000 and XDB06060300), National Natural Science Foundation of China (grants 41574079, 41174072, 41421062, and 41674097), and NASA grant NNX15AL53G. Experiments were carried out at the X17B2 beamline of the National Synchrotron Light Source and M6B at Advanced Photon Source. We thank W.B. Durham and N. Dixon for their help in preparing experiments, J. L. Mosenfelder for help on collecting FTIR spectra, W.L. Liu and D.P. Wen for help on conducting SEM-EBSD analyses, and H.Y. Chen for technical support at both beamlines. Importantly, thorough reviews by two anonymous reviewers greatly enhanced the quality of this contribution. Data used in this study can be found in Table 1. For more details, please refer to the corresponding author via e-mail contact. This is contribution No.IS-2442 from GIGCAS.

References

Bell, D. R., Ihinger, P. D., & Rossman, G. R. (1995). Quantitative analysis of trace OH in garnet and pyroxene. *American Mineralogist*, *80*, 465–474.

Bell, D. R., Rossman, G. R., Maldener, J., Endisch, D., & Rauch, F. (2003). Hydroxide in olivine: A quantitative determination of the absolute amount and calibration of the IR spectrum. *Journal of Geophysical Research*, *108*(B2), 2105. https://doi.org/10.1029/2001JB000679

Bruijn, R. H. C., & Skemer, P. (2014). Grain-size sensitive rheology of orthopyroxene. *Geophysical Research Letters*, *41*, 4894–4903. https://doi.org/10.1002/2014GL060607

Burns, R. G. (1989). Spectral mineralogy of the terrestral planets: Scanning their surfaces remotely. *Mineralogical Magazine*, *53*, 135–151.

Bystricky, M., Lawlis, J., Mackwell, S., Heidelbach, F., & Raterron, P. (2016). High-temperature deformation of enstatite aggregates. *Journal of Geophysical Research: Solid Earth*, *121*, 6384–6400. https://doi.org/10.1002/2016JB013011

Chen, S., Hiraga, T., & Kohlstedt, D. L. (2006). Water weakening of clinopyroxene in the dislocation creep regime. *Journal of Geophysical Research*, *111*, B08203. https://doi.org/10.1029/2005JB003885

Dijkstra, A. H., Drury, M. R., Vissers, R. L. M., & Newman, J. (2002). On the role of melt-rock reaction in mantle shear zone formation in the Othris Peridotite Massif (Greece). *Journal of Structural Geology*, *24*(9), 1431–1450. https://doi.org/10.1016/S0191-8141(01)00142-0

Dixon, J. E., Dixon, T. H., Bell, D. R., & Malservisi, R. (2004). Lateral variation in upper mantle viscosity: Role of water. *Earth and Planetary Science Letters*, *222*, 451–467.

Dixon, J. E., Leist, L., Langmuir, C., & Schilling, J. (2002). Recycled dehydrated lithosphere observed in plume-influenced mid-ocean-ridge basalt. *Nature*, *420*, 385–389.

Etheridge, M. A. (1975). Deformation and recrystallisation of orthopyroxene from the Giles Complex, Central Australia. *Tectonophysics*, *25*(1–2), 87–114. https://doi.org/10.1016/0040-1951(75)90012-8

Fabbrizio, A., Stalder, R., Hametner, K., Günther, D., & Marquardt, K. (2013). Experimental partitioning of halogens and other trace elements between olivine, pyroxenes, amphibole and aqueous fluid at 2 GPa and 900–1300°C. *Contributions to Mineralogy and Petrology*, *166*, 639–653. https://doi.org/10.1007/s00410-013-0902-5

Fisler, D. K., Mackwell, S. J., & Petsch, S. (1997). Grain boundary diffusion in enstatite. *Physics and Chemistry of Minerals*, *24*, 264–273. https://doi.org/10.1007/s002690050038

Gose, J., Schmadicke, E., & Beran, A. (2009). Water in enstatite from Mid-Atlantic Ridge peridotitef: Evidence for the water content of suboceanic mantle? *Geology*, *37*, 543–546. https://doi.org/10.1130/G25558A.1

Hier-Majumder, S., Mei, S., & Kohlstedt, D. L. (2005). Water weakening of clinopyroxenite in diffusion creep. *Journal of Geophysical Research*, *110*, B07406. https://doi.org/10.1029/2004JB003414

Hirth, G., & Kohlstedt, D. L. (1996). Water in the oceanic upper mantle: Implications for rheology, melt extraction and the evolution of the lithosphere. *Earth and Planetary Science Letters*, *144*, 93–108. https://doi.org/10.1016/0012-821X(96)00154-9

Hirth, G., & Kohlstedt, D. L. (2003). Rheology of the upper mantle and the mantle wedge: A view from the experimentalists, in Inside the Subduction Factory. *Geophysical Monograph Series*, *138*, 83–105. https://doi.org/10.1029/138GM06

Hitchings, R. S., Paterson, M. S., & Bitmead, J. (1989). Effects of iron and magnetite additions in olivine-pyroxene rheology. *Physics of the Earth and Planetary Interiors*, *55*(3–4), 277–291. https://doi.org/10.1016/0031-9201(89)90076-9

Huang, X., Xu, Y., & Karato, S. (2005). Water content of the mantle transition zone from electrical conductivity of wadsleyite and ringwoodite. *Nature*, *434*, 746–749.

Jiang, Z., Prior, D. J., & Wheeler, J. (2000). Albite crystallographic preferred orientation and grain misorientation distribution in a low-grade mylonite: Implications for granular flow. *Journal of Structural Geology*, *22*, 1663–1674.

Karato, S. (1992). On the Lehmann discontinuity. *Geophysical Research Letters*, *19*(22), 2255–2258. https://doi.org/10.1029/92GL02603

Karato, S. (2011). Water distribution across the mantle tranzision zone and it's implication for global material circulation. *Earth and Planetary Science Letters*, *301*, 413–423.

Karato, S., Paterson, M. S., & FitzGerald, J. D. (1986). Rheology of synthetic olivine aggregates: Influence of grain size and water. *Journal of Geophysical Research*, *91*, 8151–8176. https://doi.org/10.1029/JB091iB08p08151

Kohlstedt, D. L., Evans, B., & Mackwell, S. J. (1995). Strenght of the lithosphere: Constrain imposed by laboratory experiments. *Journal of Geophysical Research*, *100*(B9), 17,587–17,602. https://doi.org/10.1029/95JB01460

Kohlstedt, D. L., Keppler, H., & Rubie, D. C. (1996). Solubility of water in the α, β, γ phases of $(Mg,Fe)_2SiO_4$. *Contributions to Mineralogy and Petrology*, *123*, 345–357.

Kröger, F. A., & Vink, H. J. (1956). Relation between the concentrations of imperfections in crystalline solids. *Solid State Physics*, *3*, 307–435. https://doi.org/10.1016/S0081-1947(08)60135-6

Kukkonen, I. T., & Peltonen, P. (1999). Xenolith-controlled geotherm for the certral. *Fennoscandian Sheild: Implication for lithosphere-asthenosphere relations*, *304*, 301–315.

Lawlis, J. D. (1998). *High temperature creep of synthetic olivine-enstatite aggregates*, (PhD thesis). Department of Geosciences, The Pennsylvania State Univ., University Park.

Li, L., Weidner, D., Raterron, P., Chen, J. H., & Vaughan, M. (2004). Stress measurements of deforming olivine at high pressure. *Physics of the Earth and Planetary Interiors*, *143*, 357–367. https://doi.org/10.1016/j.pepi.2003.09.022

Li, Z., & Gerya, T. V. (2009). Polyphase formation and exhumation of high- to ultrahigh-pressure rocks in continental subduction zone: Numerical modeling and application to the Sulu ultrahigh-pressure terrane in eastern China. *Journal of Geophysical Research*, *114*, B09406. https://doi.org/10.1029/2008JB005935

Linckens, J., Herwegh, M., Müntener, O., & Mercolli, I. (2011). Evolution of a polymineralic mantle shear zone and the role of second phases in the localization of deformation. *Journal of Geophysical Research*, *116*, B06210. https://doi.org/10.1029/2010JB008119

Mackwell, S. J. (1991). High-temperature rheology of enstatite: Implications for creep in the mantle. *Geophysical Research Letters*, *18*, 2027–2030. https://doi.org/10.1029/91GL02492

Maggi, A., Jackson, J. A., McKenzie, D., & Priestly, K. (2000). Earthquake focal depths, effective elastic thickness, and the strength of the continental lithosphere. *Geology*, *28*(6), 495–498.

Mei, S., & Kohlstedt, D. L. (2000). Influence of water on plastic deformation of olivine aggregates: 1. Diffusion creep regime. *Journal of Geophysical Research*, *105*(B9), 21,457–21,469. https://doi.org/10.1029/2000JB900179

Mei, S., Kohlstedt, D. L., Durham, W. B., & Wang, L. (2008). Experimental investigation of the creep behavior of MgO at high pressures. *Physics of the Earth and Planetary Interiors*, *170*, 170–175. https://doi.org/10.1016/j.pepi.2008.06.030

Miyazaki, T., Sueyoshi, K., & Hiraga, T. (2013). Olivine crystals align during diffusion creep of Earth's upper mantle. *Nature*, *502*, 321–326. https://doi.org/10.1038/nature12570

Mocquet, A., Rosenblatt, P., Dehant, V., & Verhoeven, O. (2011). The deep interior of Venus, Mars, and the Earth: A brief review and the need for planetary surface-based measurements. *Planetary and Space Science*, *59*, 1048–1061. https://doi.org/10.1016/j.pss.2010.02.002

Ohuchi, T., Karato, S., & Fujino, K. (2011). Strength of single-crystal orthopyroxene under lithospheric conditions. *Contributions to Mineralogy and Petrology*, *161*, 961–975. https://doi.org/10.1007/s00410-010-0574-3

Paterson, M. S. (1982). The determination of hydroxyl by infrared-absorption in quartz, silicate-glasses anf similar materials. *Bulletin de Mineralogie*, *105*, 20–29.

Peslier, A. H., Luhr, F. J., & Post, J. (2002). Low water contents in pyroxenes from spinel-peridotites of the oxidized, sub-arc mantle wedge. *Earth and Planetary Science Letters*, *201*, 69–86.

Raleigh, C. B., Kirby, S. H., Carter, N. L., & Lallemant, H. G. A. (1971). Slip and the clinoenstatite transformation as competing rate processes in enstatite. *Journal of Geophysical Research*, *76*(17), 4011–4022. https://doi.org/10.1029/JB076i017p04011

Raterron, P., Fraysse, G., Girard, J., & Holyoke, C. W. III (2016). Strength of orthoenstatite single crysta at mantle pressure and temperature and comparison with olivine. *Earth and Planetary Science Letters*, *450*, 326–336. https://doi.org/10.1016/j.epsl.2016.06.025

Ringwood, A. E. (1975). *Composition and petrology of the earth's mantle*. New York: McGraw-Hill.

Ross, J. V., & Nielsen, K. C. (1978). High temperature flow of wet polycrystalline enstatite. *Tectonophysics*, *44*(1–4), 233–261. https://doi.org/10.1016/0040-1951(78)90072-0

Sanloup, C., Jambon, A., & Gillet, P. (1999). A simple chondritic model of Mars. *Physics of the Earth and Planetary Interiors*, *112*, 43–54. https://doi.org/10.1016/S0031-9201(98)00175-7

Singh, A. K. (1993). The lattice strains in a specimen (cubic system) compressed nonhydrostatically in an opposed anvil device. *Journal of Applied Physics*, *73*, 4278–4286. https://doi.org/10.1063/1.352809

Singh, A. K., Balasingh, C., Mao, H.-K., Hemley, R. J., & Shu, J. (1998). Analysis of lattice strains measured under nonhydrostatic pressure. *Journal of Applied Physics*, *83*, 7567–7574. https://doi.org/10.1063/1.367872

Skemer, P., & Karato, S. (2007). Effects of solute segregation on the grain-growth kinetics of orthopyroxene with implications for the deformation of the upper mantle. *Physics of the Earth and Planetary Interiors*, *164*, 186–196. https://doi.org/10.1016/j.pepi.2007.06.011

Skemer, P., & Karato, S. (2008). Sheared lherzolite xenoliths revisited. *Journal of Geophysical Research*, *113*, B07205. https://doi.org/10.1029/2007JB005286

Skemer, P. A., Warren, J. M., Kelemen, P. B., & Hirth, G. (2010). Microstructural and rheological evolution of a mantle shear zone. *Journal of Petrology*, *51*(1–2), 43–53. https://doi.org/10.1093/petrology/egp057

Sobolev, A. V., & Chaussidon, M. (1996). H_2O concentrations in primary melts from supra-subduction zones and mid-ocean ridges: Implications for H_2O storage and recycling in the mantle. *Earth and Planetary Science Letters*, *137*, 45–55. https://doi.org/10.1016/0012-821X(95)00203-O

Soustelle, V., Tommasi, A., Bodinier, J. L., Garrido, C. J., & Vauchez, A. (2009). Deformation and reactive melt transport in the mantle lithosphere above a large-scale partial melting domain: The Ronda Peridotite Massif, Southern Spain. *Journal of Petrology*, *50*(7), 1235–1266. https://doi.org/10.1093/petrology/egp032

Tasaka, M., Hiraga, T., & Zimmerman, M. E. (2013). Influence of mineral fraction on the rheological properties of forsterite + enstatite during grain-size-sensitive creep: 2. Deformation experiments. *Journal of Geophysical Research: Solid Earth*, *118*, 3991–4012. https://doi.org/10.1002/jgrb.50284

Tikoff, B., Larson, C. E., Newman, J., & Little, T. (2010). Field-based constraints on finite strain and rheology of the lithospheric mantle, Twin Sisters, Washington. *Lithosphere*, *2*(6), 418–422. https://doi.org/10.1130/L97.1

Toy, V. G., Newman, J., Lamb, W., & Tikoff, B. (2010). The role of pyroxenites in formation of shear instabilities in themantle: Evidence from an ultramafic ultramylonite, Twin Sisters Massif, Washington. *Journal of Petrology*, *51*(1–2), 55–80. https://doi.org/10.1093/petrology/egp059

Turcotte, D., & Schubert, G. (2014). *Geodynamics* (3rd ed., 636 pp.). New York: Cambridge University Press.

Warren, J. M., & Hirth, G. (2006). Grain size sensitive deformation mechanisms in naturally deformed peridotites. *Earth and Planetary Science Letters*, *248*(1–2), 438–450. https://doi.org/10.1016/j.epsl.2006.06.006

Wheeler, J. (2009). The preservation of seismic anisotropy in the Earth's mantle during diffusion creep. *Geophysical Journal International*, *178*, 1723–1732. https://doi.org/10.1111/j.1365-246X.2009.04241.x

Xu, L., Mei, S., Dixon, N., Jin, Z., Suzuki, A. M., & Kohlstedt, D. L. (2013). Effect of water on rheological properties of garnet at high temperatures and pressures. *Earth and Planetary Science Letters*, *379*, 158–165. https://doi.org/10.1016/j.epsl.2013.08.002

Zhao, Y. H., Ginsberg, S. B., & Kohstedt, D. L. (2004). Solubility of hydrogen in olivine: Dependence on temperature and iron content. *Contributions to Mineralogy and Petrology*, *147*, 155–161. https://doi.org/10.1007/s00410-003-0524-4